Chemo–Phototherapeutic Effect of Polyoxometalate-Stabilized Gold Nanostars for Cancer Treatment

Juan Ramirez Henao, Souhir Boujday, Claire Wilhelm, Basile Bouvet, Somia Tomane, Ioanna Christodoulou, Daoming Sun, Guilhem Cure, Ferdaous Ben Romdhane, Antoine Miche, et al.

Chemo-Phototherapeutic Effect of Polyoxometalate-Stabilized Gold Nanostars for Cancer Treatment

Juan F. Ramirez Henao,[a,b] Souhir Boujday,[b] Claire Wilhelm,[c] Basile Bouvet,[a] Somia Tomane,[a,b] Ioanna Christodoulo,[b] Daoming Sun,[b] Guilhem Cure,[c] Ferdaous Ben Romdhane,[d] Antoine Miche,[b] Anne Dolbecq,[a] Pierre Mialane[a] and Anne Vallée[a,b]*

[a] Institut Lavoisier de Versailles (ILV), UMR CNRS 8180, UVSQ, Université Paris-Saclay, 45, avenue des Etats-Unis, 78035 Versailles Cedex, France.

[b] Sorbonne Université, Laboratoire de Réactivité de Surface (LRS), UMR CNRS 7197, 4 place Jussieu, 75252 Paris, France.

[c] Institut Curie, Université PSL, Sorbonne Université, CNRS UMR168, Laboratoire Physico Chimie Curie, 75005 Paris, France.

[d] Fédération de Chimie et Matériaux de Paris-Centre (FCMat), Campus Pierre et Marie Curie, 4 Place Jussieu, F-75005 Paris, France.

KEYWORDS: nanoparticles, Gold nanostars, Polyoxometalate, Hyperthermia, Cancer treatment

ABSTRACT: A reduced polyoxometalate (POM) functionalized with bisphosphonate (BP) ligands possessing antitumoral properties was used to synthesize metallic gold nanostars (AuNS) with high reproducibility through a silver-assisted seed growth method. Notably, this study is the first to employ a reduced polyoxometalate as a dual-function reducing and capping agent in the synthesis of gold nanostars. The resulting AuNS@POM composites, characterized by a plasmon band located at 744 nm, combine in a single hybrid nanocomposite alendronate ligands, Mo(VI) ions and Au^0 centers. The colloidal stability of AuNS@POM was demonstrated in a biological culture medium and cell experiments were performed to study its anti-tumor activity on U87 and MCF7 cell lines from glioblastoma and liver cancer, respectively. First, it was established that the anti-tumoral activity of the BP POM is enhanced due to the Mo(V) to Mo(VI) oxidation process that occurs during AuNSs formation. Second, it has been shown that in the presence of the composite, cellular metabolic activity decreases drastically under the effect of irradiation at 808 nm, even leading to almost complete cell death. AuNS@POM therefore exhibits strong anti-tumor chemo-photothermal activity, paving the way for the development of a new type of dual therapeutic agent operating under near infrared irradiation.

INTRODUCTION

Cancer is one of the major health challenges facing humanity today.[1,2] Despite the extensive effort to fight cancer, traditional treatments have significant side effects and limited efficacy, making the development of new therapeutic strategies urgent. In this way, nanotherapies, based on nanoscale delivery systems as vehicles for antineoplastic agents, have attracted much attention these past few years thanks to their potential for targeting and multifunctionality.[3,4] Liposomes, dendrimers, carbon nanotubes or quantum dots-based nanosystems have been considered as nanocarriers for cancer diagnosis or treatments.[5] Amongst inorganic nanosystems, gold nanoparticles (AuNPs) have been the most widely studied and can be seen as state-of-the-art actors for biomedical applications due to their low toxicity and the possibility to implement combinatorial therapy to reach an optimized global therapeutic effect.[6] In particular, the combination of chemotherapy, resulting from the functionalization of the gold nanoparticles with drugs or bioactive small molecules, and the intrinsic plasmonic properties of gold, allowing the use of photothermal therapy (PTT) in which light is used to treat cancer cells, is emerging as an important dual therapy alternative.[7] AuNPs functionalized with active organic species such as fluorouracil, folic acid, doxorubicin, paclitaxel or daunorubicin have thus been investigated.[8] In contrast, AuNPs functionalized with biologically active inorganic molecules have been much less studied. Among the different families of inorganic molecules to consider, the appeal of polyoxometalates (POMs) stands out prominently.[9–12] POMs, which can be seen as negatively charged molecular oxides based on metals in high oxidation states (typically $W^{VI,V}$, $Mo^{VI,V}$ or $V^{V,IV}$), can exhibit significant antitumoral activities with putative proposed mechanisms of action, the most frequently discussed being affecting the activity of different enzymes.[13–15] As early as 1988, Yamase and co-workers have indeed shown that the simple $[NH_3Pr^i]_6[Mo_7O_{24}]$ (Pr^i = isopropyl) polyoxomolybdate was efficient *in vitro* and *in vivo* by suppressing the tumor growth in mice,[16] the activity of this POM being comparable to

fluorouracil. Following this pioneering work, a wide variety of inorganic POMs have been investigated, including polyoxotungstates and polyoxovanadates. Nevertheless, the primary attention within the realm of bioactive POMs currently revolves around hybrid organic-inorganic polyoxometalates.[17] The incorporation of organic groups connected to the inorganic core has indeed the potential to reduce toxicity and enhance cell penetration capabilities.[13,17] Furthermore, this approach allows the biological activity of the POM to be combined with that of the chosen organic moiety in a single molecule. In this context, some of us reported on the antitumoral activity of a series of POMs structured by biologically relevant bisphosphonate (BP) ligands, showing for example that a polyoxomolybdate incorporating a Mn(III) center and the antitumoral zoledronate BP, namely $[(Mo^{VI}_2O_6)_2(Zol)_2Mn^{III}]^{5-}$ (Mo_4Zol_2Mn with Zol = $[O_3PC(C_4H_6N_2)OPO_3]^{5-}$), is highly active against SK-ES-1 sarcoma cells in mouse xenograft systems due to a synergistic effect between the POM and the BP, with no noticeable cytotoxicity.[18] In this context, we recently reported the design of core/shell AuNP@Mo_4Zol_2Mn nanohybrids consisting of pre-formed spherical gold nanoparticles functionalized by the Mo(VI) Mo_4Zol_2Mn POM.[19] Anticancer activity investigations against PC3 human prostate adenocarcinoma cells evidenced that the high antitumor activity of the hybrid POM was preserved in this composite. Moreover, PTT treatments performed under 680 nm irradiation showed a decrease of 50 % in the metabolic activity of the PC3 cells at a concentration where the composite exhibited no anticancer activity in the dark. However, to optimize the efficiency of combined chemo/phototherapies, it is essential to control the shape of the NPs so that they have a large surface area to promote high drug loading and a plasmonic band with maximum absorption in the near infrared (NIR), which is ideal for safe and deep penetration into tissue. Gold nanostars (AuNSs) are the nanoparticles of choice to meet these two criteria,[20] although, to our knowledge, AuNS/POM composites have never been reported.

In the following, we use for the first time a reduced POM functionalized with BP ligands and exhibiting antitumoral properties as both a reducing and capping agent to produce hybrid nanocomposites combining AuNS and POM-BP (AuNS@POM), and assess their anti-tumoral activity against two types of cancer cell lines. We describe the engineering and in-depth characterization of these hybrid nanocomposites obtained from the reduced bisphosphonate polyoxometalate $[Mo^{V}_4O_8(Ale)_2]^{4-}$ (Mo_4Ale_2, with Ale = alendronate = $[O_3PC(C_3H_6NH_3)OPO_3]^{5-}$) whose antitumoral activity had been previously evidenced.[21] This POM is built from the connection of four $Mo^{V}O_6$ octahedra by two alendronate ligands (Figure S1). We leverage the distinctive properties of this hybrid polyoxomolybdate in a dual capacity. Firstly, we harness its antitumor attributes for therapeutic applications. Secondly, we explore its efficacy as a reducing agent for gold nanoparticles, made possible by the presence of Mo(V) ions, an aspect underexplored in the current literature.[22–26] In addition, in the synthetic process adopted, the POM also acts as stabilizing agent by surrounding the nanostars. We can emphasize that while a wide variety of synthetic methods using non-biocompatible surfactants, which limit their clinical application, have been reported for the preparation of AuNS, only two surfactant-free routes have been published.[27,28] Finally, cell experiments were performed to investigate in the dark and under NIR irradiation the antitumoral activity against MCF-7 breast cancer and U87 glioblastoma cell lines of the fully characterized AuNS@POM composites.

RESULTS AND DISCUSSION

Scheme 1 describes the synthetic route adopted for the engineering of the AuNS@POM composite. This synthesis route is a two-stage process. In a first step, spherical gold seeds were prepared using citrate ions as reducing and stabilizing agents, following the Turkevitch method.[29] The seed suspension exhibits a localized surface plasmon resonance (LSPR) band situated at 520 ± 1 nm (Figure S2a) and a red color (Figure S2b), in accordance with the

transmission electron microscopy (TEM) observation of spherical gold nanoparticles of 15 ± 1 nm diameter (Figures S2c and S2d). Next, a growth step was performed by adding a solution of $HAuCl_4 \cdot 3H_2O$ at 4°C to the seed suspension acidified to pH 2.6, followed by silver nitrate which promotes anisotropic growth of the NPs,[30] and finally the Mo_4Ale_2 POM, which acts as a reducing and stabilizing agent.

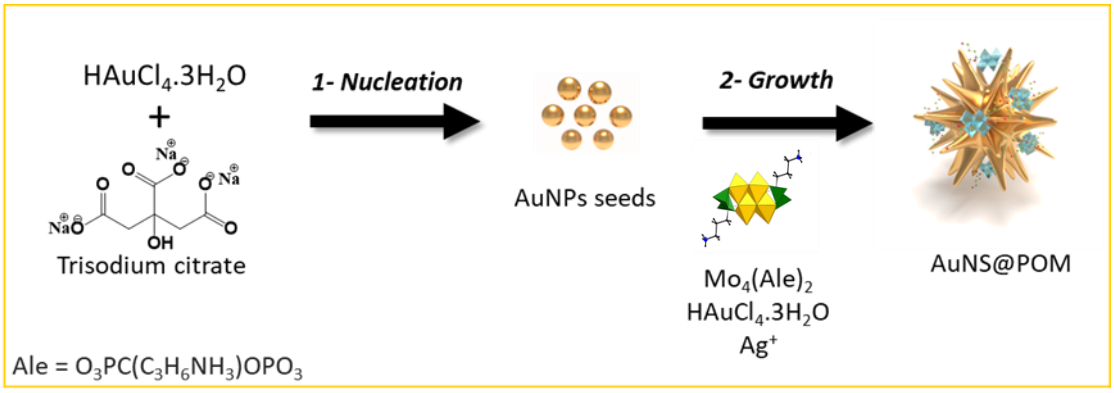

Scheme 1 : Schematic representation of the AuNS@POM synthetic pathway.

The AuNS synthesis was performed with an Au seeds concentration of 0.173 nM and monitored by UV-Visible spectroscopy and TEM. Figure 1 shows the evolution of the absorption spectra of the colloidal synthetic medium as a function of reaction time.

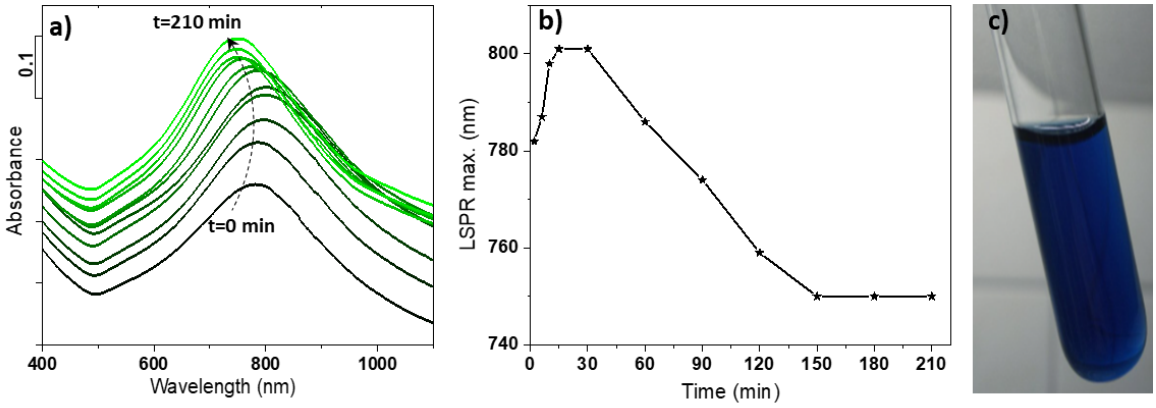

Figure 1. (a) Optical characterization of the AuNS@POM colloidal synthetic medium over 210 minutes reaction and (b) related maximum wavelength plasmon band evolution; (c) picture of the final colloidal suspension.

A LSPR band was observed at 782 nm after two minutes of reaction. The absorbance of this band then increased rapidly over the first 25 minutes, accompanied by a red shift at 800 nm. After a short plateau, the LSPR band underwent a progressive blue shift which stabilized at 744 ± 10 nm after 150 minutes, suggesting the completion of the reaction. Such a two-step growth process has already been observed for PVP-assisted synthesis of AuNSs,[31,32] with the first step consisting of a rapid growth of the tips, followed by the preferential deposition of gold on the central core. However, it should be noted that it is the first time that gold nanostars are obtained directly from reduced POMs using the silver-assisted seed growth method. The synthesis protocol led to a highly reproducible optical response of the AuNSs, as shown by the UV spectra of different batches obtained by different experimenters of the laboratory (Figure S3a). Finally, the excess of POM at the surface of the NPs was removed by appropriate washings and monitored by UV-Vis spectroscopy (Figure S3b). The absorbance at 290 nm (A_{290}), characteristic of the Mo_4Ale_2 POM, was measured and divided by A_{744}, the absorbance of the LSPR band. The decrease of the A_{290}/A_{744} ratio from 2.4 (before washing) to 1.5 (after washing) highlights the removal of excess POM. The resulting nanostars are particularly stable, the absorption spectrum of the colloidal solution showing no wavelength shift and only a 14% decrease in absorbance after one month (Figure S4).

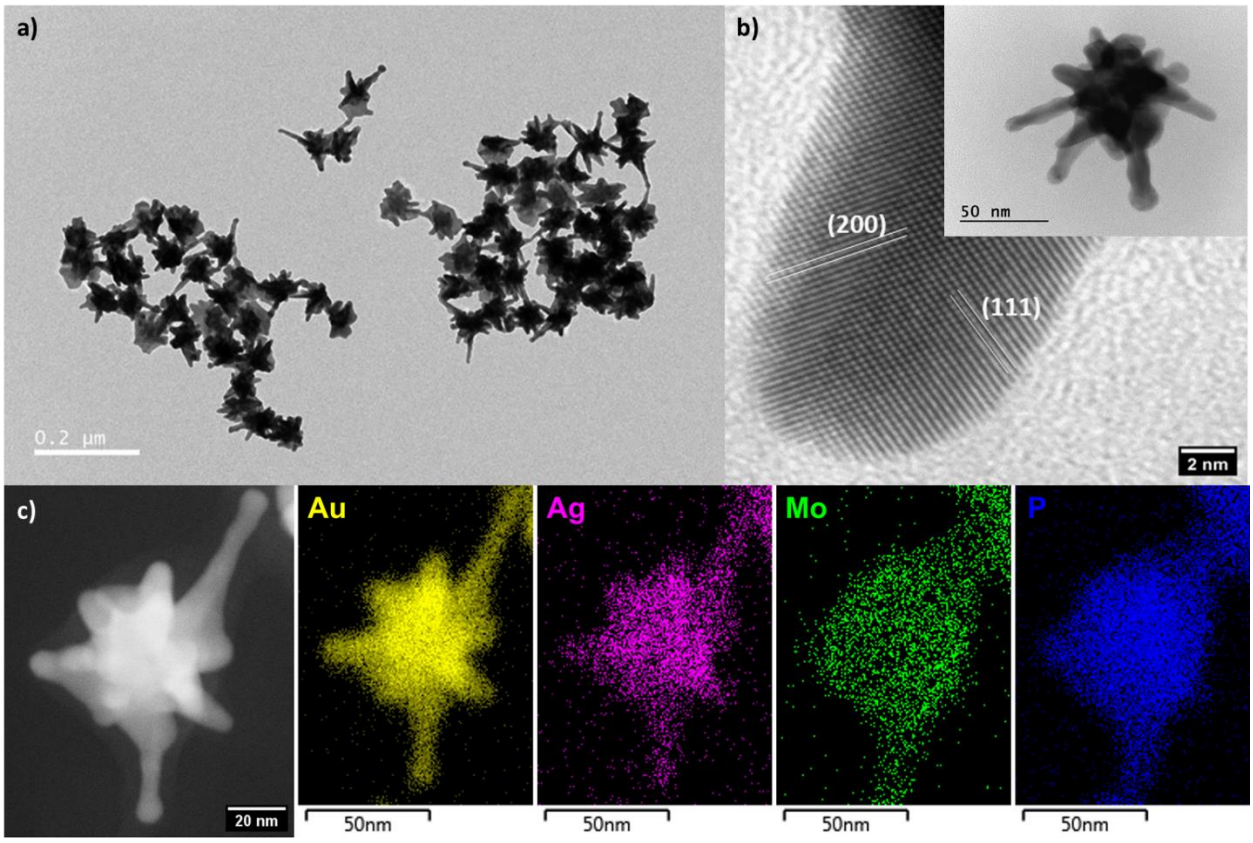

Figure 2. (a) TEM image of AuNS@POM; (b) HRTEM image of a single tip of a AuNS@POM (inset); (c) HAADF STEM image of a AuNS@POM and related STEM-EDS elemental mapping images.

TEM and HRTEM images shown in Figure 2a and 2b, show that the morphology of AuNS@POM nanohybrids is characterized by a core diameter of 40 ± 8 nm and tip lengths of 35 ± 11 nm. We can underline that the AuNS@POM size could be modulated by varying the concentration of Au seeds. Indeed, by decreasing the Au seeds concentration from 0.173 to 0.008 nM, the core diameter increased from 40 to 110 nm and the tips length from 35 to 139 nm, respectively (see experimental details and Figure S5 in the SI). The difference of contrast around the nanostars observed by the high-angle annular dark field scanning transmission electron microscopy (HAADF-STEM) image (Figure 2c) can be attributed to the POM layer surrounding the star core. STEM-EDS elemental mapping images indeed show the presence of

P and Mo atoms in this layer, with a homogeneous distribution around the Au/Ag NS core. In the STEM-EDS elemental mapping images, Ag is present on the surface of the AuNs, as well as on the tips. As previously demonstrated for syntheses using a similar Ag(I) concentration, the silver layer deposited by an underpotential mechanism seems to contribute stabilizing the nanostars.[33,34] EDX measurements indicate a Mo/P ratio of 0.94±0.2 in excellent agreement with the expected one (Mo/P = 1 in Mo_4Ale_2). Besides, the layer thickness, of ca. 7 nm, is indicative of a multi-layer assembly of POMs around the NS core. The AuNS@POM composites were also characterized by dynamic light scattering (DLS), the hydrodynamic particle size being estimated to 93 ± 3 nm. This value, consistent with the size measured by TEM as it includes the hydration layer, points out the absence of aggregation of nanoparticles in colloidal suspension. This good stability is maintained by an efficient electrostatic repulsion as suggested by the significantly negative zeta potential (-33 ± 12 mV), resulting from the negative charge of the POMs coating the NSs.

Further analysis via IR (Figure S6)**,** Raman (Figure S7) and XPS (Figure S8) confirmed the presence of POMs in the nanohybrid. The IR spectrum of AuNS@POM indeed shows the characteristic bands of the hybrid POM, with P-O vibrations at 1160 and 1064 cm^{-1} together with Mo=O and Mo-O vibrations at 941 and 898 cm^{-1} (see Table S1), respectively, and Raman data are consistent with the observations obtained by IR (Table S2). Figure S8 shows the Mo 3d XPS spectra of Mo_4Ale_2 and AuNS@POM, respectively. The spectrum of Mo_4Ale_2 presents a doublet with a Mo 3d 5/2 component at 231.2 eV and a Mo 3d 3/2 component at 234.4 eV, characteristic of a Mo(V) compound. The spectrum of AuNS@POM could only be fitted considering that both Mo(V) and Mo(VI) species were present, with Mo(VI) 3d 5/2 and Mo(VI) 3d 3/2 photopeaks located at 232.8 and 236.0 eV, respectively. However, integration evidenced that the molybdenum has been almost entirely oxidized during the synthetic process, with a Mo(VI):Mo(V) ratio of 95:5, confirming the role of the Mo(V) centers as reducing agents.

Finally, the POM layer completely dominates the XPS signal, attenuating the signal of gold, in agreement with the thick layer observed by HAADF. However, the formation of AuNSs in presence of POM was confirmed by PXRD (Figure S9).

Inductively coupled plasma optical emission spectroscopy (ICP-OES) was performed before and after the AuNS@POM washing process. For both the unwashed and washed samples, an experimental Mo/P ratio of 1.0 ± 0.1 was found, in agreement with the Mo/P ratio in the Mo_4Ale_2 precursor and confirming the EDX measurements (see above). Nevertheless, the exact structure of the oxidized POM cannot be determined precisely, and for the study of the biological activities (see below), we have used as a reference compound the Mo(VI) POM $[(Mo^{VI}_3O_8)_2O(Ale)_2]^{6-}$ (Mo_6Ale_2, Figure S1), which is easy to synthesize and very stable in solution.[35] Besides, Ale/Au ratios decreased from 3.5± 0.1 to 1.3± 0.6 upon washing. The former ratio is close to the proportion of gold and POM introduced in the synthetic media, while the latter evidences that POMs have been released in solution during the washing step. It is particularly interesting to note that this value is very close to the ratio obtained by calculating the amount of POM required to reduce Au ions during synthesis, *i.e.* 1.44. But overall, both XPS, STEM-EDS mapping, IR spectroscopy and ICP-OES results evidenced that POMs play the role of reducing agents of gold ions and remain at the surface of the AuNSs, with the same composition although the oxidation state of molybdenum is different, to ensure the colloidal stability.

Before assessing the activity against cancer cells, the stability of AuNS@POM at two different concentrations (corresponding to [Ale] = 25 and 100 µM, respectively) in DMEM (Dulbecco's Modified Eagle Medium) culture medium was evaluated via electronic absorption spectroscopy, DLS and cryo-TEM (Figure 3). Firstly, and within the first five minutes, the UV-Vis spectra recorded in DMEM (Figures 3a and 3b) showed a red shift of the LSPR band of 14 and 54 nm at the lowest and highest concentrations, respectively. This reflects the formation of

a protein corona around the AuNS@POM in the biological medium. This protein corona formation is also suggested by the increase in particle size evidenced by DLS (Figure 3c) as well as by cryo-TEM images (Figures 3d and 3e) obtained after one day. The protein corona determined by cryo-TEM is thicker (44.3 ± 9.1 nm) for the highest concentration compared to 22.5 ± 4.8 nm for the lowest concentration, in agreement with UV-Vis spectra. Overall, it should be emphasized that no particle aggregation process was observed for at least five days in the biological medium, with the position of the LSPR band and the size of the AuNS@POM composite measured by DLS stabilizing after 24 hours.

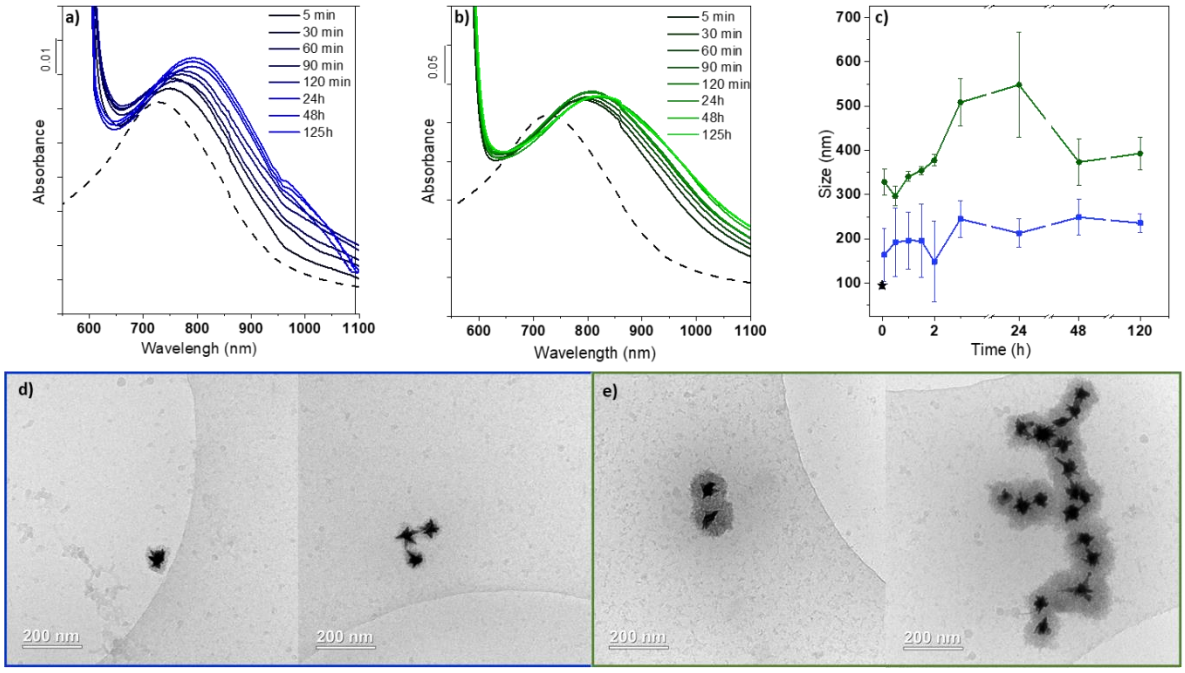

Figure 3. Evolution with time in the 0-125 h range of the UV-Vis spectrum of AuNS@POM in DMEM at a) 25 µM and b) 100 µM Ale concentrations (full lines). Dotted lines: UV-Vis spectrum of AuNS@POM in water at a) 25 µM and b) 100 µM Ale concentrations; c) Evolution with time in the 0-120 h range of the particle size as determined by DLS in DMEM at 25 µM (light blue) and 100 µM (dark blue) Ale concentrations; Cryo-TEM images after 24 h in DMEM for d) [Ale] = 25 µM and e) 100 µM.

Two different cancerous cell lines, Glioblastoma U87 and MCF7, were selected to evaluate the therapeutic performances at different extracellular concentrations in alendronate for Mo_4Ale_2 and AuNS@POM incubated during 1 or 5 days. The previously reported compound Mo_6Ale_2,[35] which is related to the Mo_4Ale_2 POM but incorporates molybdenum ions only in the +VI oxidation state (see above), was also tested to obtain a better accuracy when estimating the input of the oxidized form of the POMs around the AuNS@POM. It has indeed previously been shown that the oxidation state of molybdenum ions can play a significant role in the anti-cancer activity of hybrid polyoxomolybdates.[21,35] For AuNS@POM, the samples were both investigated in absence and under irradiation with a 808 nm laser calibrated at 1.7 W/cm^2 to estimate the PTT activity. Alamar blue assays were used to determine the metabolic activity. The IC_{50} of the different components were deduced from the dose-response curves (

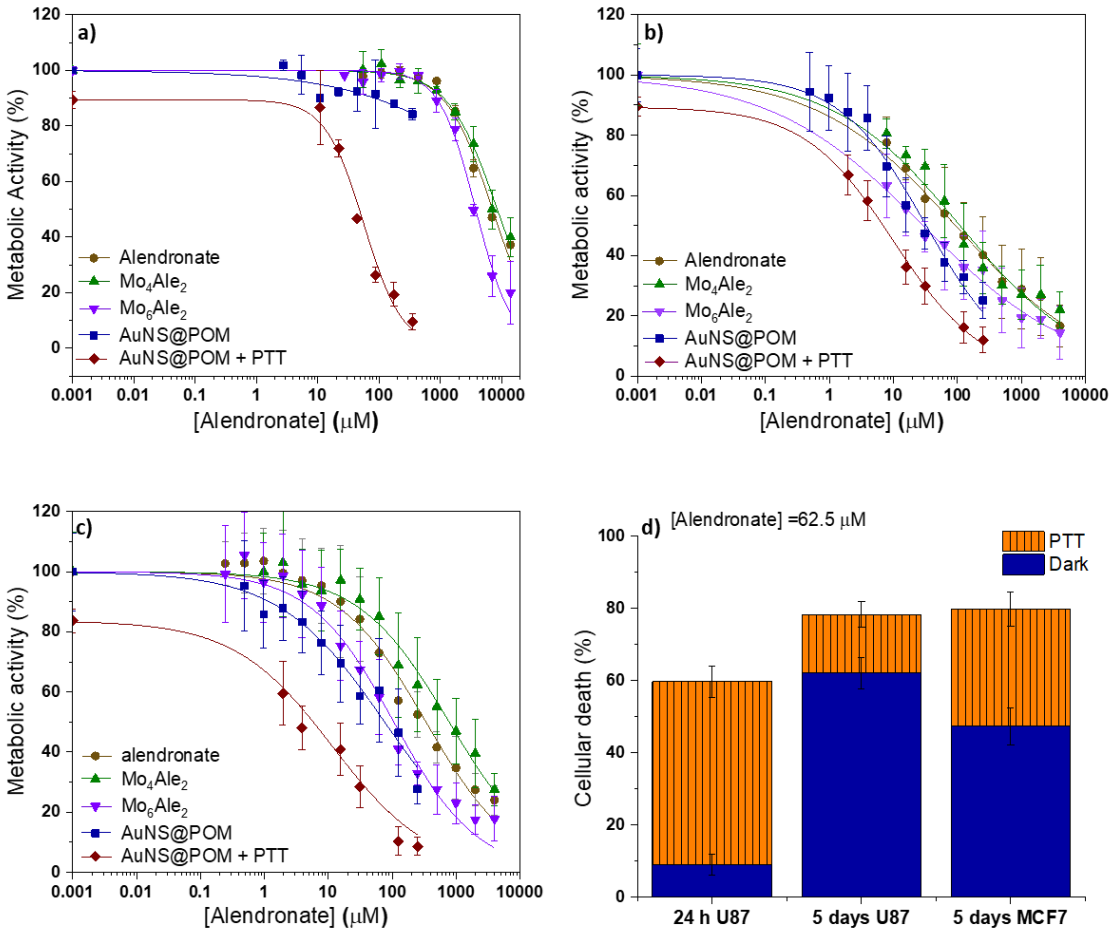

Figure **4**), and are summarized in Table 1. Note that for all the curves shown in Figure 4 the metabolic activity starts at 100 % at 0 µM alendronate, i.e. in the absence of any additive, except when the cells are irradiated where a slight decrease is observed (10 to 17%), showing that the irradiation moderately impacts the cells viability.

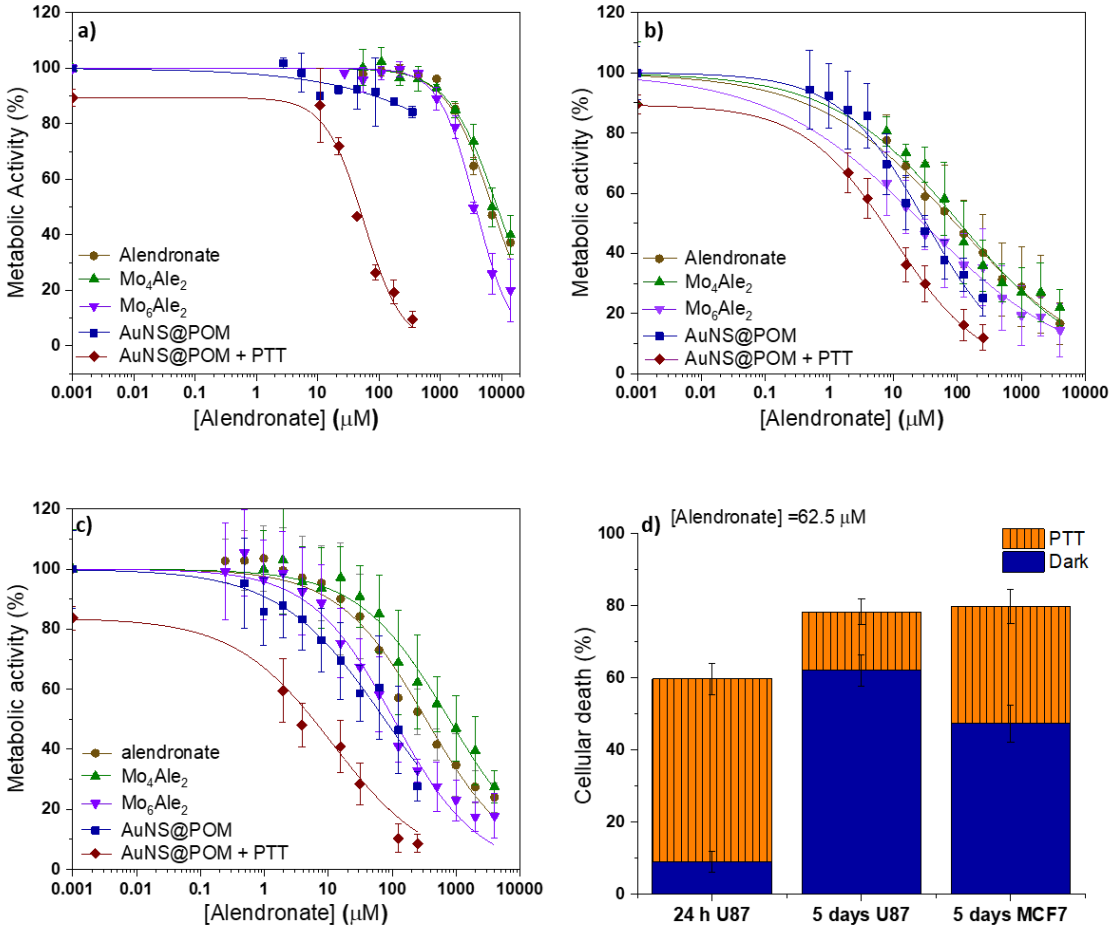

Figure 4. Dose-response curves of the metabolic activity per alendronate (yellow curve): U87 cells incubated during 24 h (a) and five days (b), or MCF7 cells incubated during five days (c) with Mo_4Ale_2 (green curve), Mo_6Ale_2 (purple curve) and AuNS@POM under the presence (wine curve, PTT) or absence (blue curve) of irradiation (808 nm); d) histograms showing the respective contributions of chemotherapy (blue) and PTT under 860 nm irradiation (wine) on U87 and MCF7 cells death for AuNS@POM with alendronate concentration of 62.5 µM.

Table 1. IC_{50} values per alendronate at 1 and 5 days for the Mo_4Ale_2, Mo_6Ale_2 and AuNS@POM species.

	U87 IC_{50}^{24h} [μM] per alendronate	U87 IC_{50}^{5days} [μM] per alendronate	MCF7 IC_{50}^{5days} [μM] per alendronate
alendronate	7090 ± 360	93 ± 14	340 ± 40
Mo_4Ale_2	8500 ± 660	110 ± 15	780 ± 110
Mo_6Ale_2	3800 ± 200	29 ± 6	106 ± 10
AuNS@POM	-	32 ± 4	76 ± 15
AuNS@POM +PTT	47 ± 4	7 ± 1	6 ± 2

First, Glioblastoma U87 cells were incubated in DMEM for 24 hours (Figure 4a). The dose-response curves for free alendronate and Mo_4Ale_2 overlapped significantly with similar IC_{50} values, indicating that Mo_4Ale_2 retained the antitumor activity of alendronate. However, the chemotherapeutic activity of alendronate and Mo_4Ale_2 was very low after 24 h, with an IC_{50} of 7090 and 8500 μM, respectively. In contrast, Mo_6Ale_2 exhibited a higher chemotherapeutic activity, with an IC_{50} of 3800 μM. This confirms that Mo(VI) species possess a better antitumoral activity, while Mo(V) ones do not show significant chemotherapeutic effects. The chemotherapeutic activity after 24 h of the AuNS@POM nanocomposites could be evaluated only for concentrations lower than 125 μM per alendronate, i.e. at lower concentrations than the pure POMs. Indeed, the evaluation of the AuNS@POM activity for higher concentrations was inaccessible because of the impossibility to further concentrate the colloidal suspensions while maintaining colloidal stability. Nevertheless, this initial trend suggests that AuNSs preserve and possibly enhance the therapeutic effect of the molybdenum (VI) bisphosphonates species. More importantly, under irradiation at 808 nm, the IC_{50} measured for AuNS@POM falls down to ~50 μM *i.e.* 150 times lower than free alendronate, demonstrating the high impact

of the photothermal effect of these nanostructures.

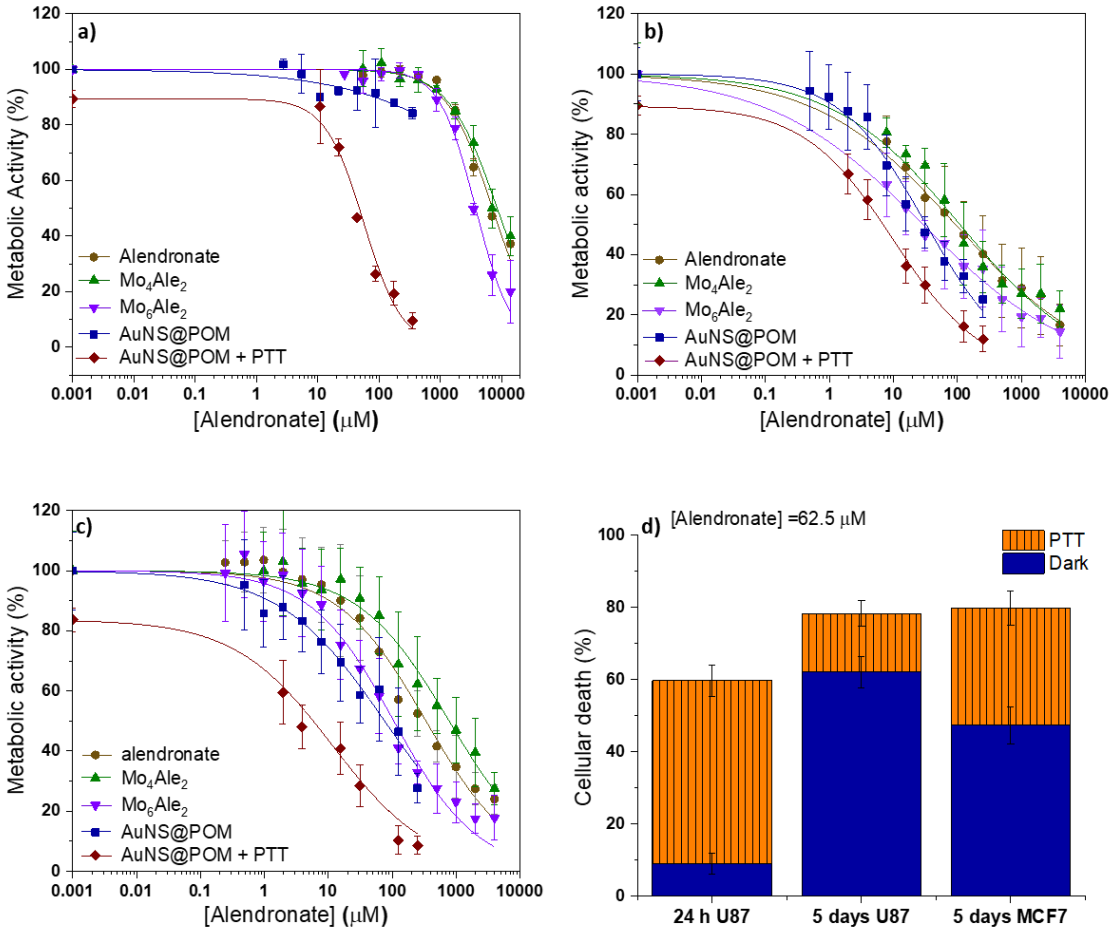

Figure 4b shows the dose-response curves obtained after 5 days of contact with the Glioblastoma U87 cells. The resulting IC_{50} are reported in Table 1. Whatever the chemotherapeutic agent tested, it is clear that the IC_{50} decreased sharply after five days of incubation compared with 24 h, showing that the chemotherapeutic effect is time-dependent. The chemotherapeutic activity of alendronate and Mo_4Ale_2 reached an IC_{50} of ~ 100 µM, 8 times lower than upon 24 h contact, while Mo_6Ale_2 and AuNS@POM exhibited a remarkable IC_{50} of ~ 30 µM. Here again, under irradiation at 808 nm, the IC_{50} measured for AuNS@POM drastically decreases to ~7 µM.

To better apprehend the effect of irradiation on the activities of AuNS@POM, we plotted U87 cells death without and under irradiation in the near infrared (Figure 4d). At an extracellular alendronate concentration of 62.5 µM and after 24 hours incubation, AuNS@POM showed only a very low anti-cancer activity, with ca. 9 % cell death. It is striking to note that metabolic activity falls drastically under irradiation at 808 nm, with 59 % cell death. At the same concentration but for five days of incubation in the dark, an anticancer activity of 60 % was reached, while in the same conditions but under irradiation, an almost complete cell death was observed. This clearly evidenced that AuNS@POM acts as a dual chemo-photothermal therapeutic agent.

The antitumoral activities of alendronate, Mo_4Ale_2, Mo_6Ale_2 and AuNS@POM were also evaluated considering another cell line, the MCF7 (

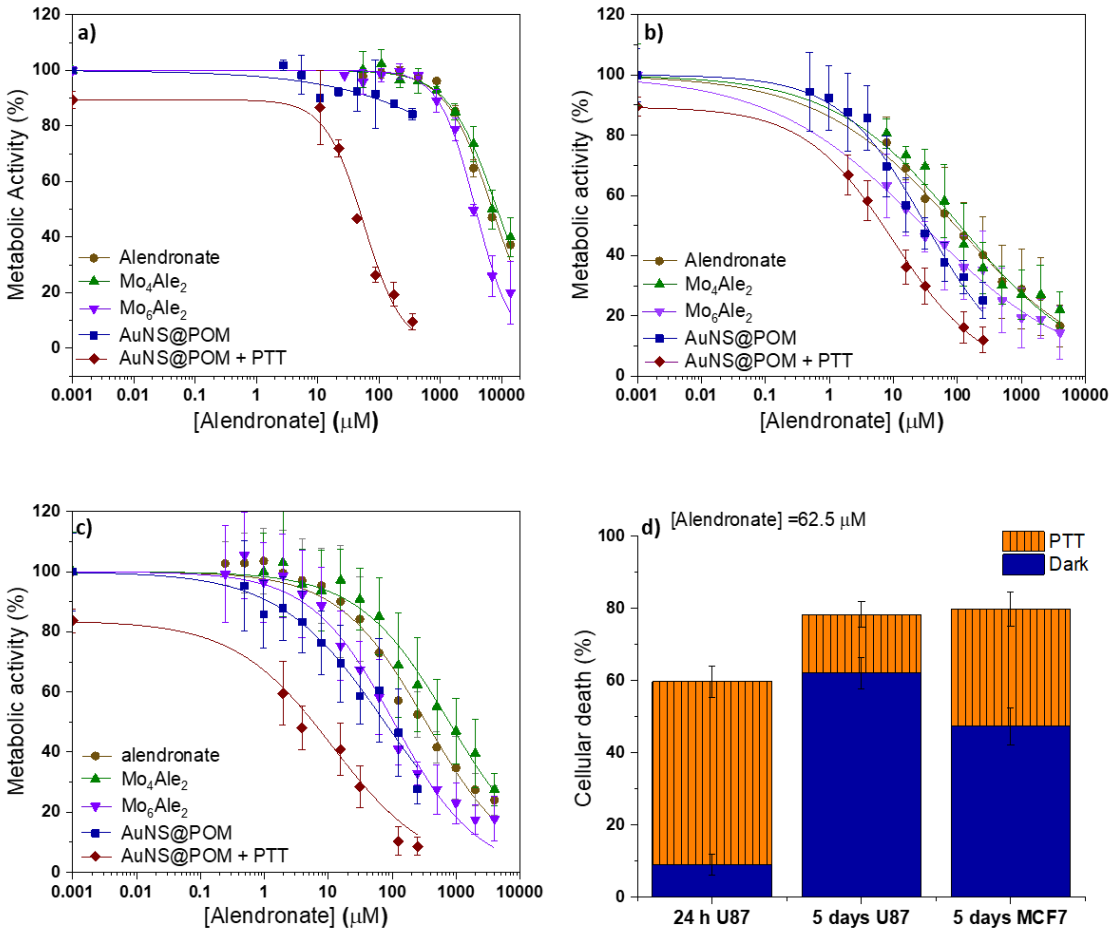

Figure **4**c). After five days of incubation in DMEM and in absence of irradiation, the alendronate molecules and composites were overall less active against this cell line, with, for all the tested molecules/composites, an IC_{50} 2 to 7 times higher than that measured for the U87 cell line for similar incubation time. Yet, when comparing the responses within the cell line MCF7, the same trends were observed as for the U87 ones: alendronate and Mo_4Ale_2 had the lowest activities while the Mo_6Ale_2 and AuNS@POM IC_{50} values were close, although the nanocomposite had a slightly better activity (Table 1). The input of irradiation was even more striking in this case as the IC50 decreased down to 6 μM, i.e. approx. 12 times lower than without irradiation. Figure 4d shows that, as with U87 cells at an extracellular alendronate concentration of 62.5 μM, almost complete cell death was observed after five days of incubation followed by irradiation at 808 nm, confirming the dual chemo-photothermal therapeutic role of AuNS@POM.

Overall, it can be noted that the PTT effect is stronger than that observed for the spherical composite AuNP@Mo_4Zol_2Mn,[19] highlighting the influence of the morphology of the gold nanoparticles (stars versus spheres).

The toxicity of Mo_6Ale_2 and the AuNS@POM was also evaluated on non-cancerous MCF10 cells, after 120h of incubation (Figure S10). The dose-response curves for the two compounds overlapped, confirming that when Mo is in oxidation state VI, the POM activity is similar to that of the AuNS@POM. Furthermore, it is notable that the metabolic activity is similar on non-cancerous and cancerous cells, which is often observed for many chemotherapeutic agents.[36] For future applications, it will therefore be necessary to administer the drug in a targeted manner by intra-tumoral injection.

To better understand the mechanisms involved, we investigated the input of the NSs on the internalization process by performing ICP measurements on washed cells isolated from batches incubated for 5 days with Mo_4Ale_2, Mo_6Ale_2 and AuNS@POM, respectively, at an alendronate

concentration of 62.5 µM. For the three chemotherapeutic agents, similar internalization in U87 incubated cells were observed (Figure S11), indicating that the better activity of AuNS@POM compared to the pristine Mo_4Ale_2 POM is not the result of a better internalization in the cells but comes from the Mo(V)/Mo(VI) oxidation process occurring during the synthesis. It should be noted that contrary to what was observed for the U87 cell line, better internalization was demonstrated for AuNS@POM compared to Mo_4Ale_2 or Mo_6Ale_2 for the MCF-7 cell line. This might explain the higher difference in activity between AuNS@POM and Mo_4Ale_2 for this cell line compared to U87.

Additionally, TEM images of U87 and MCF7 cells cultured during five days with AuNS@POM at 7.8 µM and 62.5 µM concentrations in alendronate and after irradiation are shown in Figure S12. These images highlight for the two cell lines that the AuNSs were confined in the endosomal compartments of the cells after endocytosis pathway internalization. This result also demonstrates that increasing the dose leads to an increase of the number of endosomes containing the nanoparticles and an increase of the density of the nanoparticles within the endosomes. The percentage of gold internalized in the cells determined via ICP after cells washing is the same for the two cell lines at 7.8 µM and 62.5 µM concentrations in alendronate (*ca.* 60%). Remarkably, AuNS@POMs internalization clearly demonstrates cell death, with almost complete destructuration of the cell bodies and fragmentation of the nuclei, particularly for the high dose, and for both cell lines.

Conclusion

AuNS@POMs hybrid nanocomposites combining gold nanostars and bisphosphonates-containing polyoxometalates possessing a chemotherapeutic potential were synthesized for the first time and tested as anti-tumoral agents against two cancer cell lines. In addition, these hybrid nanocomposites absorb in the near infrared and thus offer a high potential for

photothermal therapy against cancer and therefore lead to a combined chemo and phototherapeutic activity. AuNS@POM have been isolated using an innovative synthetic route involving a POM combining molybdenum centres and alendronate ligands, chemo-therapeutically active for cancer treatment, with the hybrid POM acting as reducing and stabilising agent. An in-depth investigation of the synthesis conditions allowed to optimize the parameters leading to highly-reproducible AuNS@POM with well-defined branches. XPS, ICP and X-EDS analysis enabled to quantify the amount of POM capping the AuNSs and determine the molybdenum oxidation state which has a major impact on the antitumoral activity of such hybrids. The antitumoral activity of the AuNS@POM was assessed on two cell lines, MCF7 and U87, and was significantly greater than that of pristine Mo(V) hybrid POM. In addition, the antitumoral activity of AuNS@POM was drastically enhanced under irradiation in the NIR region, leading to almost total cellular death. These results demonstrate the promising potential of such nanostructures as chemo/photothermal agents and highlight the importance of three factors on the antitumoral activities of the hybrid nanocomposites: i) the morphology of the nanoparticles (nanostars versus nanospheres), ii) the oxidation state of the molybdenum ions of the POM and iii) the irradiation in the near infrared. The efficiency of these hybrid nanocomposites paves the way for their broader use as dual photo and chemo-therapeutic agents for cancer treatment.

ASSOCIATED CONTENT

Supporting Information. Additional characterization results.

AUTHOR INFORMATION

Corresponding Author

* Anne Vallée : anne.vallee@sorbonne-universite.fr

Author Contributions

The manuscript was written through contributions of all authors. All authors have given approval to the final version of the manuscript.

Funding Sources

This work was supported by the Ministère de l'Enseignement Supérieur et de la Recherche, the CNRS, the Université de Versailles Saint Quentin en Yvelines, the Sorbonne University and a public grant overseen by the French National Research Agency (ANR) as part of the "Investissements d'Avenir" program no. ANR-11-IDEX-0003-02 and CHARMMMAT ANR-11-LABX-0039 and European Union, project ERC-2019-CoG project NanoBioMade 86562.

Acknowledgments

The authors thank Jean-Michel Guigner and Nicolas Menguy at Institut de Minéralogie, de Physique des Matériaux et de Cosmochimie (IMPMC) for cryo-TEM processing, Michel Salmain and Benoît Bertrand for their help in running toxicity tests on healthy cells. Flavien Bourdreux is gratefully acknowledged for his assistance in running ICP measurements.

MATERIALS AND METHODS

Materials. Sodium citrate, gold(III) chloride trihydrate, silver nitrate, hydrazine hydrate, molybdenum (VI) oxide, hydrochloric acid, diethylamine were purchased from Sigma-Aldrich. Ammonia solution (32% in water) was obtained from VWR. Mo_4Ale_2 and Mo_6Ale_2[21,35] were synthesized as previously described.

Synthesis

Synthesis of Mo_4Ale_2 and Mo_6Ale_2

Briefly Mo_4Ale_2[21] and Mo_6Ale_2[35] were synthesized as previously described. For Mo_4Ale_2, hydrazine hydrate ($N_2H_4 \cdot H_2O$) was introduced into a suspension of MoO_3 in aqueous HCl. After a 3-hour warming period, alendronic acid was dissolved in the solution, and diethylamine was subsequently added until reaching a pH of 7. Small red crystals were obtained through filtration the following day. For Mo_6Ale_2, Ammonium molybdate tetrahydrate $(NH_4)_6Mo_7O_{24} \cdot 4H_2O$ and Alendronic acid were dissolved in water, and HCl was added until the solution reached pH 2.5. Then, RbCl was added as a solid, leading to a precipitate. After filtration, the solid was dissolved in NH_4OAc/AcOH buffer and the solution left to evaporate slowly at room temperature for few days, affording big needle-shaped crystals. Mo_4Ale_2 and Mo_6Ale_2 have been characterized by IR and NMR spectroscopies. Comparison of the data obtained with those reported in the literature confirms the purity of the compounds used in this study.

Mo_4Ale_2: I.R. spectroscopy: $\nu(cm^{-1})$ = IR: =1558 (w), 1452 (s), 1392 (w), 1164 (w), 1137 (vs), 1114 (m), 1033 (m), 1026 (s), 968 (vs), 937 (s), 891 (w), 846 (w), 813 (m), 732(s), 702 (m), 673 cm^{-1} (m);

^{31}P NMR (300 MHz, D_2O, 25 °C): δ 30.8 and 20.0 (AB spin system, ^2J = 23.4 Hz).

Mo_6Ale_2: I.R. spectroscopy: $\nu(cm^{-1})$ = 1502 (w), 1415 (s br), 1144 (s), 1122 (s), 1072 (s), 1053(w), 1020 (s), 983 (w), 910 (m), 883 (w), 863 (m), 825 (w), 729 (s), 687 cm^{-1} (m). ^{31}P NMR (300 MHz, D_2O, 25 °C): δ 22.36 (s, 1.8 P), 22.07 (s, 0.2 P).

Synthesis of gold Nanostars (AuNS): AuNS@POM was synthesized via a two steps seed-mediated method. The seed solution was prepared by adding 106 µL of a 5% (0.17 M) aqueous citrate sodium solution to 15 mL of a 0.3 mM $HAuCl_4,3H_2O$ aqueous solution at 100°C with stirring. The solution turned black, then red. After 7 minutes, the solution was quickly cooled using an ice bath. The obtained seeds were stored in an amber glass bottle at 4°C for later use.

For the growth step, 100 µL of aqueous 0.1 M HCl was added to 4.75 mL of a 0.5 mM $HAuCl_4$ solution in an ice-water mix bath. Next, 300 µL of the seed solution was added, followed 30 seconds later by the addition of 100 µL of an aqueous 4 mM silver nitrate solution, and finally 20 seconds later 50 µL of a 0.1 M Mo_4Ale_2 aqueous solution was added. After a few minutes, the colour of the solution turned deep blue. Stirring was stopped after 2 hours and the nanostars were simultaneously washed and concentrated by centrifugation at 2000 RPM for 12 minutes in glass tubes. The supernatant was then removed and replaced with ultrapure water. These two steps were repeated twice. The obtained AuNS@POM composite was stored in an amber glass bottle at 4°C for later use. For the analysis of the seed's concentration effect, the seeds were diluted 5, 10 and 20 times in ultrapure water before being added in order to add exactly the same amount of solution.

Characterization Techniques

FTIR spectroscopy measurements were performed on a Nicolet 30 ATR 6700 FT spectrometer with scan range from 4000 to 400 cm^{-1}.

Powder X-Ray diffractograms (PXRD) were measured on a Siemens D5000 Diffractometer working in Bragg-Brentano geometry [(θ-2θ) mode] in the 2θ range 2.5–60°, by using CuKα radiation (λKα = 1.5406 Å).

UV-Visible spectra were recorded on a PerkinElmer Lambda 750 with scan range from 350 to 1200 cm^{-1}.

Dynamic Light Scattering: Batch mode hydrodynamic size (diameter) measurements were performed on a Malvern Zetasizer Nano ZS. A minimum of three measurements per sample were made.

Zeta Potential Measurements: A Malvern Zetasizer Nano ZS instrument was used to measure zeta potential at 25°C for all samples. Samples prepared for the DLS measurements were loaded into a pre-rinsed folded capillary cell for the zeta potential measurements. A minimum of three measurements per sample were made.

Inductively Coupled Plasma Optical Emission Spectrometry: The P, Mo and Au contents for POMs, composites and cells were determined on samples digested in aqueous solution using an Agilent Technologies 700 Series ICP-OES instrument. The digestion procedure was carried out by adding a 0.5 mL mixture of HCl:HNO_3 in a 2:1 ratio to 0.5 mL of the nanoparticle solution for 4 hours at 80°C, and then left overnight at room temperature. The following day, each sample was mixed with ultrapure water to obtain a total volume of 6 mL.

For the cells, after the supernatant was removed, 200 μL of the same HCl:HNO_3 mixture was added to each plate and heated at 80°C for 4 hours and then left overnight at room temperature. The following day, each sample was mixed with ultrapure water to obtain a total volume of 4 mL.

X-Ray Photoelectron Spectroscopy: XPS analyses were performed using an Omicron Argus X-ray photoelectron spectrometer, equipped with a monochromated AlKα radiation source (hν = 1486.6 eV) and a 280 W electron beam power. The emission of photoelectrons from the sample was analyzed at a takeoff angle of 45° under ultra-high vacuum conditions ($\leq 10^{-9}$ mBar). Spectra were carried out with a 100 eV pass energy for the survey scan and 20 eV pass energy for the Mo 3d region. Binding energies were calibrated against the C 1s (C-C) binding energy at 284.8 eV and element peak intensities were corrected by Scofield factors. The peak areas were determined after subtraction of a Shirley background. The spectra were fitted using Casa XPS v.2.3.15 software (Casa Software Ltd, U.K.) and applying a Gaussian-Lorentzian (70%/30%) functions.

Transmission Electron Microscopy: Transmission electron microscopy (TEM) images were collected using a JEOL JEM-1011 microscope operating at an accelerating voltage of 100 kV. The TEM grids were prepared by depositing 10 µL of a particle suspension on a carbon-coated copper grid and dried at room temperature. High-resolution transmission electron microscopy (HRTEM) measurements were carried out using a JEOL 2100Plus UHR microscope operating at 200 kV. Scanning transmission electron microscopy (STEM) images using a high-angle annular dark-field (HAADF) detector were also acquired. STEM mode coupled with X-ray Energy-Dispersive Spectroscopy (X-EDS) was used to perform elemental mapping. X-EDS analysis was realized with an Oxford Instrument SDD detector of 80 mm^2. X-ray spectra were recorded and processed with Aztec software. The nanoparticles size distributions were calculated by measuring a minimum of 200 particles using the ImageJ software. For TEM imaging of cellular samples, after incubation with nanoparticles, the cells were detached with trypsin and fixed in 5% glutaraldehyde diluted in 0.1 M cacodylate buffer for 1 hour and washed with cacodylate buffer. Samples were then contrasted with Oolong Tea Extract (OTE) cacodylate buffer, followed by post-fixation with 1% osmium tetroxide and 1.5% potassium cyanoferrate. A series of dehydration baths, from 30% to 100% were then performed before embedding the cell pellets in epoxy resins. The resins were finally sectioned (70 nm), and sections were placed on cooper grids for observation with a Hitachi HT 7700 TEM operating at 80 kV

The Cryo-TEM grids were prepared by deposing 10 µL of a particle suspension on a carbon-coated copper grid and freezing by immersion on liquid ethane and the excess was removed. Measurements were realized in a JEOL JEM-2100 microscope operating at an accelerating voltage of 100 kV.

Cytotoxicity assay: Nanoparticles were internalized by U87 and MCF7 cells in a 96-well plate for 5 days and with U87 for 24 hours. Six conditions were compared. Firstly, cells were kept in

culture for 24 hours or 5 days as control condition. Secondly, culture medium was enriched with alendronate molecules, with concentrations ranging from 0.24 µM to 4 mM. Thirdly, culture medium was enriched with Mo_4Ale_2 at concentrations comprised between 1 µM to 1.5 mM in alendronate. Fourthly, culture medium was enriched with Mo_6Ale_2 at concentrations comprised between 0.24 µM to 1.5 mM in alendronate. Fifthly culture medium was enriched with AuNS@POM at concentrations comprised between 0.48 µM to 0.25 mM in alendronate. Finally, cells supplemented with AuNS@POM were exposed to a laser 806 nm at 1.7 W/cm^2 during 5 minutes. In a previous study by some of us, this 1.7 W/cm^2 laser power was efficient to induce tumor growth inhibition in vivo without exhibiting nonspecific phototoxicity.[37] In addition, this value is lower than the power used in many in vivo studies.[38–40]

After 24 hours or 5 days, the culture medium was replaced by 200 µL of RPMI without phenol red, supplemented with 10% Alamar Blue. After 2 hours the plate was analyzed with a multimode plate reader (Enspire Perkin Elmer) at an excitation wavelength of 570 nm and a fluorescence detection at 585 nm. Metabolic activity was determined by comparison with control cells.

Metabolic activity fits:

All fits are adjusted using a Levenberg–Marquardt algorithm to represent the DoseResp model[4142] with variable Hill slope (p) disponible in OriginPro software presented in Eq.1

$$y = A1 + \frac{A_2 - A_1}{1+10^{(Log\, x_0 - x)p}} \qquad (1)$$

A1 is the bottom asymptote representing the maximum effectivity of the drug with an "infinite concentration" and A2 is the top asymptote that represent the activity without the treatment.

Log x_0 is the logarithm of the concentration when the activity is the half of the maximum activity (note that x_0 is the logarithm of the IC_{50}).

x is the independent variable of the fit (-9.0, -2.4): the log of the concentration of the drug in moles/L.

y is the dependent variable [0,100]: percentage of metabolic activity

p is the variable Hill slope. For p>0 the metabolic activity is stimulated by the medicament and for p<0 it's inhibited. $|p| > 1$ indicates a steeper slope.

References

(1) GLOBOCAN 2018: Counting the Toll of Cancer. *Lancet* **2018**, *392* (10152), 985. https://doi.org/10.1016/S0140-6736(18)32252-9.

(2) Bray, F.; Ferlay, J.; Soerjomataram, I.; Siegel, R. L.; Torre, L. A.; Jemal, A. Global Cancer Statistics 2018: GLOBOCAN Estimates of Incidence and Mortality Worldwide for 36 Cancers in 185 Countries. *CA. Cancer J. Clin.* **2018**, *68* (6), 394–424. https://doi.org/10.3322/caac.21492.

(3) Ediriwickrema, A.; Saltzman, W. M. Nanotherapy for Cancer: Targeting and Multifunctionality in the Future of Cancer Therapies. *ACS Biomater. Sci. Eng.* **2015**, *1* (2), 64–78. https://doi.org/10.1021/ab500084g.

(4) Bajpai, S.; Tiwary, S. K.; Sonker, M.; Joshi, A.; Gupta, V.; Kumar, Y.; Shreyash, N.; Biswas, S. Recent Advances in Nanoparticle-Based Cancer Treatment: A Review. *ACS Appl. Nano Mater.* **2021**, *4* (7), 6441–6470. https://doi.org/10.1021/acsanm.1c00779.

(5) Yao, Y.; Zhou, Y.; Liu, L.; Xu, Y.; Chen, Q.; Wang, Y.; Wu, S.; Deng, Y.; Zhang, J.; Shao, A. Nanoparticle-Based Drug Delivery in Cancer Therapy and Its Role in Overcoming Drug Resistance. *Front. Mol. Biosci.* **2020**, *7* (August), 1–14. https://doi.org/10.3389/fmolb.2020.00193.

(6) Sztandera, K.; Michałand, G.; Klajnert-Maculewicz, B. Gold Nanoparticles in Cancer Treatment. *Mol. Pharm.* **2019**, *16* (1), 1–23. https://doi.org/10.1021/acs.molpharmaceut.8b00810.

(7) Riley, R. S.; Day, E. S. Gold Nanoparticle-Mediated Photothermal Therapy: Applications and Opportunities for Multimodal Cancer Treatment. *Wiley Interdiscip. Rev. Nanomedicine Nanobiotechnology* **2017**, *9* (4), e1449. https://doi.org/10.1002/wnan.1449.

(8) Jahangirian, H.; Kalantari, K.; Izadiyan, Z.; Rafiee-Moghaddam, R.; Shameli, K.; Webster, T. J. A Review of Small Molecules and Drug Delivery Applications Using Gold and Iron Nanoparticles. *Int. J. Nanomedicine* **2019**, *14*, 1633–1657. https://doi.org/10.2147/IJN.S184723.

(9) Miras, H. N.; Yan, J.; Long, D. L.; Cronin, L. Engineering Polyoxometalates with Emergent Properties. *Chem. Soc. Rev.* **2012**, *41* (22), 7403–7430. https://doi.org/10.1039/c2cs35190k.

(10) Miras, H. N.; Vilà-Nadal, L.; Cronin, L. Polyoxometalate Based Open-Frameworks (POM-OFs). *Chem. Soc. Rev.* **2014**, *43* (16), 5679–5699. https://doi.org/10.1039/c4cs00097h.

(11) Soria-Carrera, H.; Atrián-Blasco, E.; Martín-Rapún, R.; Mitchell, S. G. Polyoxometalate-Peptide Hybrid Materials: From Structure-Property Relationships to Applications. *Chem. Sci.* **2022**, *14* (1), 10–28. https://doi.org/10.1039/d2sc05105b.

(12) Dolbecq, A.; Dumas, E.; Mayer, C. R.; Mialane, P. Hybrid Organic-Inorganic Polyoxometalate Compounds: From Structural Diversity to Applications. *Chem. Rev.* **2010**, *110* (10), 6009–6048. https://doi.org/10.1021/cr1000578.

(13) Bijelic, A.; Aureliano, M.; Rompel, A. Polyoxometalates as Potential Next-Generation Metallodrugs in the Combat Against Cancer. *Angew. Chemie - Int. Ed.* **2019**, *58* (10), 2980–2999. https://doi.org/10.1002/anie.201803868.

(14) Chang, D.; Li, Y.; Chen, Y.; Wang, X.; Zang, D.; Liu, T. Polyoxometalate-Based Nanocomposites for Antitumor and Antibacterial Applications. *Nanoscale Adv.* **2022**, *4* (18), 3689–3706. https://doi.org/10.1039/D2NA00391K.

(15) Čolović, M. B.; Lacković, M.; Lalatović, J.; Mougharbel, A. S.; Kortz, U.; Krstić, D. Z. Polyoxometalates in Biomedicine: Update and Overview. *Curr. Med. Chem.* **2019**, *27*

(3), 362–379. https://doi.org/10.2174/092986732666190827153532.
(16) Yamase, T.; Fujita, H.; Fukushima, K. Medical Chemistry of Polyoxometalates. Part 1. Potent Antitumor Activity of Polyoxomolybdates on Animal Transplantable Tumors and Human Cancer Xenograft. *Inorganica Chim. Acta* **1988**, *151* (1), 15–18. https://doi.org/10.1016/S0020-1693(00)83477-5.
(17) Zhang, H.-Z.; Zhao, H.-X.; Chang, W.-H.; Liu, X.-Y.; Chen, P.; Yu, A.-Q.; Chishti, A. N.; Zhang, Y.-Z.; Ni, L.-B.; Wang, X.-Q.; Wei, Y.-G. Hetero-Bimetallic Transition Metal-Substituted Krebs-Type Polyoxometalate with N-Chelating Ligand as Anticancer Agents. *Tungsten* **2023**, *5* (2), 225–234. https://doi.org/10.1007/s42864-023-00210-8.
(18) Boulmier, A.; Feng, X.; Oms, O.; Mialane, P.; Rivière, E.; Shin, C. J.; Yao, J.; Kubo, T.; Furuta, T.; Oldfield, E.; Dolbecq, A. Anticancer Activity of Polyoxometalate-Bisphosphonate Complexes: Synthesis, Characterization, in Vitro and in Vivo Results. *Inorg. Chem.* **2017**, *56* (13), 7558–7565. https://doi.org/10.1021/acs.inorgchem.7b01114.
(19) Tomane, S.; Wilhelm, C.; Boujday, S.; Fromain, A.; Miche, A.; Bourdreux, F.; Dolbecq, A.; Mialane, P.; Vallée, A. Gold/Polyoxometalate Core/Shell Nanoparticles for Combined Chemotherapy-Photothermal Cancer Therapy. *ACS Appl. Nano Mater.* **2021**, *4* (3), 2339–2344. https://doi.org/10.1021/acsanm.0c03187.
(20) Fabris, L. Gold Nanostars in Biology and Medicine: Understanding Physicochemical Properties to Broaden Applicability. *J. Phys. Chem. C* **2020**. https://doi.org/10.1021/acs.jpcc.0c08460.
(21) Compain, J. D.; Mialane, P.; Marrot, J.; Sécheresse, F.; Zhu, W.; Oldfield, E.; Dolbecq, A. Tetra- to Dodecanuclear Oxomolybdate Complexes with Functionalized Bisphosphonate Ligands: Activity in Killing Tumor Cells. *Chem. - A Eur. J.* **2010**, *16* (46), 13741–13748. https://doi.org/10.1002/chem.201001626.
(22) Tomane, S.; López-Maya, E.; Boujday, S.; Humblot, V.; Marrot, J.; Rabasso, N.; Castells-Gil, J.; Sicard, C.; Dolbecq, A.; Mialane, P.; Vallée, A. One-Pot Synthesis of a New Generation of Hybrid Bisphosphonate Polyoxometalate Gold Nanoparticles as Antibiofilm Agents. *Nanoscale Adv.* **2019**, *1* (9), 3400–3405. https://doi.org/10.1039/c9na00401g.
(23) Lang, Z.; Gabas, I. M.; Lopez, X.; Clotet, A.; de la Fuente, J. M.; Mitchell, S. G.; Poblet, J. M. On the Formation of Gold Nanoparticles from [AuIIICl4]– and a Non-Classical Reduced Polyoxomolybdate as Electron Source: Quantum Mechanical Modelling and Experimental Study. *New J. Chem.* **2016**, *40* (2), 1029–1038. https://doi.org/10.1039/C5NJ02773J.
(24) Zhang, S.; Liu, R.; Li, S.; Dolbecq, A.; Mialane, P.; Suo, L.; Bi, L.; Zhang, B.; Liu, T.; Wu, C.; Yan, L.; Su, Z.; Zhang, G.; Keita, B. Simple and Efficient Polyoxomolybdate-Mediated Synthesis of Novel Graphene and Metal Nanohybrids for Versatile Applications. *J. Colloid Interface Sci.* **2018**, *514*, 507–516. https://doi.org/10.1016/j.jcis.2017.12.039.
(25) Barbero, F.; Michelini, S.; Moriones, O. H.; Patarroyo, J.; Rosell, J.; F. Gusta, M.; Vitali, M.; Martín, L.; Canals, F.; Duschl, A.; Horejs-Hoeck, J.; Mondragón, L.; Bastús, N. G.; Puntes, V. Role of Common Cell Culture Media Supplements on Citrate-Stabilized Gold Nanoparticle Protein Corona Formation, Aggregation State, and the Consequent Impact on Cellular Uptake. *Bioconjug. Chem.* **2022**, *33* (8), 1505–1514. https://doi.org/10.1021/acs.bioconjchem.2c00232.
(26) Martín, S.; Takashima, Y.; Lin, C. G.; Song, Y. F.; Miras, H. N.; Cronin, L. Integrated Synthesis of Gold Nanoparticles Coated with Polyoxometalate Clusters. *Inorg. Chem.* **2019**, *58* (7), 4110–4116. https://doi.org/10.1021/acs.inorgchem.8b03013.

(27) Yuan, H.; Khoury, C. G.; Hwang, H.; Wilson, C. M.; Grant, G. A.; Vo-Dinh, T. Gold Nanostars: Surfactant-Free Synthesis, 3D Modelling, and Two-Photon Photoluminescence Imaging. *Nanotechnology* **2012**, *23* (7), 75102. https://doi.org/10.1088/0957-4484/23/7/075102.

(28) Chandra, K.; Culver, K. S. B.; Werner, S. E.; Lee, R. C.; Odom, T. W. Manipulating the Anisotropic Structure of Gold Nanostars Using Good's Buffers. *Chem. Mater.* **2016**, *28* (18), 6763–6769. https://doi.org/10.1021/acs.chemmater.6b03242.

(29) Zabetakis, K.; Ghann, W. E.; Kumar, S.; Daniel, M. C. Effect of High Gold Salt Concentrations on the Size and Polydispersity of Gold Nanoparticles Prepared by an Extended Turkevich-Frens Method. *Gold Bull.* **2012**, *45* (4), 203–211. https://doi.org/10.1007/s13404-012-0069-2.

(30) Atta, S.; Beetz, M.; Fabris, L. Understanding the Role of AgNO 3 Concentration and Seed Morphology in the Achievement of Tunable Shape Control in Gold Nanostars. *Nanoscale* **2019**, *11* (6), 2946–2958. https://doi.org/10.1039/c8nr07615d.

(31) Khoury, C. G.; Vo-Dinh, T. Gold Nanostars for Surface-Enhanced Raman Scattering: Synthesis, Characterization and Optimization. *J. Phys. Chem. C* **2008**, *112* (48), 18849–18859. https://doi.org/10.1021/jp8054747.

(32) Pu, Y.; Zhao, Y.; Zheng, P.; Li, M. Elucidating the Growth Mechanism of Plasmonic Gold Nanostars with Tunable Optical and Photothermal Properties. *Inorg. Chem.* **2018**, *57* (14), 8599–8607. https://doi.org/10.1021/acs.inorgchem.8b01354.

(33) Tsoulos, T. V.; Atta, S.; Lagos, M. J.; Beetz, M.; Batson, P. E.; Tsilomelekis, G.; Fabris, L. Colloidal Plasmonic Nanostar Antennas with Wide Range Resonance Tunability. *Nanoscale* **2019**, *11* (40), 18662–18671. https://doi.org/10.1039/c9nr06533d.

(34) De Silva Indrasekara, A. S.; Johnson, S. F.; Odion, R. A.; Vo-Dinh, T. Manipulation of the Geometry and Modulation of the Optical Response of Surfactant-Free Gold Nanostars: A Systematic Bottom-Up Synthesis. *ACS Omega* **2018**, *3* (2), 2202–2210. https://doi.org/10.1021/acsomega.7b01700.

(35) El Moll, H.; Dolbecq, A; Mbomekallé, I. M.; Marrot, J.; Deniard, P.; Dessapt, R.; Mialane, P. Tuning the photochromic properties of molybdenum bisphosphonate polyoxometalates. *Inorg. Chem.* **2012**, *51* (4), 2291–2302. https://doi.org/10.1021/ic202299d.

(36) Fraczkowska, K.; Bacia, M.; Przybyło, M.; Drabik, D.; Kaczorowska, A.; Rybka, J.; Stefanko, E.; Drobczynski, S.; Masajada, J.; Podbielska, H.; Wrobel, T.; Kopaczynska, M. Alterations of Biomechanics in Cancer and Normal Cells Induced by Doxorubicin. *Biomed. Pharmacother.* **2018**, *97*, 1195–1203. https://doi.org/https://doi.org/10.1016/j.biopha.2017.11.040.

(37) Plan Sangnier, A.; Preveral, S.; Curcio, A.; K. A. Silva, A.; Lefèvre, C. T.; Pignol, D.; Lalatonne, Y.; Wilhelm, C. Targeted Thermal Therapy with Genetically Engineered Magnetite Magnetosomes@RGD: Photothermia Is Far More Efficient than Magnetic Hyperthermia. *J. Control. Release* **2018**, *279* (January), 271–281. https://doi.org/10.1016/j.jconrel.2018.04.036.

(38) Von Maltzahn, G.; Park, J. H.; Agrawal, A.; Bandaru, N. K.; Das, S. K.; Sailor, M. J.; Bhatia, S. N. Computationally Guided Photothermal Tumor Therapy Using Long-Circulating Gold Nanorod Antennas. *Cancer Res.* **2009**, *69* (9), 3892–3900. https://doi.org/10.1158/0008-5472.CAN-08-4242.

(39) Dickerson, E. B.; Dreaden, E. C.; Huang, X.; El-Sayed, I. H.; Chu, H.; Pushpanketh, S.; McDonald, J. F.; El-Sayed, M. A. Gold Nanorod Assisted Near-Infrared Plasmonic Photothermal Therapy (PPTT) of Squamous Cell Carcinoma in Mice. *Cancer Lett.* **2008**, *269* (1), 57–66. https://doi.org/10.1016/j.canlet.2008.04.026.

(40) Feng, Y.; Chang, Y.; Sun, X.; Cheng, Y.; Zheng, R.; Wu, X.; Wang, L.; Ma, X.; Li, X.; Zhang, H. Differential Photothermal and Photodynamic Performance Behaviors of Gold Nanorods, Nanoshells and Nanocages under Identical Energy Conditions. *Biomater. Sci.* **2019**, *7* (4), 1448–1462. https://doi.org/10.1039/c8bm01122b.
(41) Beaumont, N.; Hancox, I.; Sullivan, P.; Hatton, R. A.; Jones, T. S. Increased Efficiency in Small Molecule Organic Photovoltaic Cells through Electrode Modification with Self-Assembled Monolayers. *Energy Environ. Sci.* **2011**, *4* (5), 1708–1711. https://doi.org/10.1039/c1ee00005e.
(42) Jones, G. Fitting and Handling Dose Response Data. *J. Comput. Aided. Mol. Des.* **2015**, *29* (1), 1–11. https://doi.org/10.1007/s10822-014-9752-0.

Graphical abstract